Journal of the European Ceramic Society **42** (2022) p4594–4606

Microstructure-property relationships in composites of 8YSZ ceramics and *in situ* graphitized nanocellulose

Polona Hudelja[a,b], Rainer Schmidt[c,d], Harvey Amorín[e], Sandra Drev[f], Aljaz Ivekovic[a], Anze Abram[a], Andraz Kocjan[a,*], Bernd Wicklein[e]

[a] *Department for Nanostructured Materials, Jožef Stefan Institute, Jamova 39,1000 Ljubljana, Slovenia*
[b] *Jožef Stefan International Postgraduate School, Jamova 39, 1000 Ljubljana, Slovenia*
[c] *Facultad de Ciencias Físicas, GFMC, Universidad Complutense de Madrid, 28040 Madrid, Spain*
[d] *Laboratorio de Heteroestructuras con aplicación en spintrónica, Unidad asociadaUCM/CSIC, 28049 Madrid, Spain*
[e] *Materials Science Institute of Madrid (ICMM), Consejo Superior de Investigaciones Científicas (CSIC), Sor Juana Inés de la Cruz 3, 28049 Madrid, Spain*
[f] *Center for Electron Microscopy and Microanalysis, Jožef Stefan Institute, Jamova 39, 1000 Ljubljana, Slovenia*

* Corresponding author. Email address: a.kocjan@ijs.si (A. Kocjan).

ABSTRACT

Keywords:
YSZ
Nanocellulose
Ceramic matrix composite
Graphitization
Sintering
Conductivity

Ceramic matrix composites (CMC) of 8 mol.% yttria-stabilized zirconia (8YSZ) mixed with natural fiber nano-cellulose (0.75, 1, 2 wt%) were prepared by spark plasma sintering (SPS). Nanocellulose markedly improved the densification of the 8YSZ ceramic matrix and induced significant grain size refinement. It was demonstrated that *in situ* graphitization of nanocellulose during the SPS processing resulted in 6 nm thin turbostratic graphite layers homogeneously covering the 8YSZ ceramic grains. The dielectric properties were analyzed by electrical impedance spectroscopy suggesting a low percolation threshold near or below ≈ 1.6 vol% graphite, above which mixed ionic-electronic conduction dominates. The CMCs are stable under reducing conditions (5%H_2/Ar at-mosphere) at least until 800 °C with a high conductivity of $\sigma_{dc} = 0.17\ \mathrm{Scm}^{-1}$ even at 900 °C (8YSZ-2% CNF). These features make the 8YSZ-nanocellulose CMCs promising candidates for application in medium- to high- temperature electrochemical devices.

1. Introduction

Yttria-stabilized zirconia (YSZ) ceramics are commonly used in industrial applications such as thermal barrier coatings, fuel cells and catalysis technology [1–3]. The transport, thermal and mechanical properties of YSZ ceramics are strongly correlated with the attained density and microstructure, providing a powerful lever for tuning the properties of YSZ [4–6]. In fully dense 8 mol.% yttria-stabilized zirconia (8YSZ) ceramics, higher ionic conductivity [7], lower thermal conduc-tivity [8] and higher mechanical strength [9] can be achieved by decreasing the grain size to the nanoscale.

An alternative strategy to conveniently adjust the properties of YSZ may be the fabrication of so-called ceramic matrix composites (CMC). In general, the fabrication of CMC allows the introduction of redox, catalytic and magnetic properties to a ceramic matrix by the addition of the appropriate transition metal oxide nanoparticles (e.g. NiO or Fe_2O_3), while thermal, electronic and mechanical properties may be best modified by adding nanocarbons (e.g. carbon nanotubes, carbon nanofibers or graphene) [10,11].

In both cases, successful consolidation and sintering are crucial. Microwave sintering and two-step sintering are well-known techniques to achieve submicron-sized dense 8YSZ ceramics [7,12,13]. More recently, Spark Plasma Sintering (SPS) (sometimes alternatively called Field Assisted Sintering Technology (FAST) or Pulsed Electric Current Sintering (PECS)) has emerged as an interesting sintering technique for the densification of pure 8YSZ [4,5,9,12,14], and 8YSZ-based CMCs containing carbon nanofillers [15–17]. In both cases, mechanical pres-sure and pulsed electrical currents are applied under vacuum. However, obtaining fully dense 8YSZ ceramics with low grain size using SPS processes is still challenging due to high grain boundary mobility and ionic conductivity [5,1218]. Therefore, the addition of carbon nano-fillers to ceramic 8YSZ matrices may offer a two-fold advantage: *i)* They may well contribute to the microstructural refinement and *ii)* enhance the functional and the (micro)structural properties of 8YSZ.

Concerning the former, mechanical pressure applied during SPS contributes to the densification via local plastic deformation of grain contact points allowing grain sliding [19], where nanocarbons may act as lubricant and further promote densification. In the final sintering stages nanocarbons will pin the grain boundaries and, in this way, limit the extensive grain growth process. Thus, achieving densities close to theoretical values of 8YSZ CMCs using SPS is possible [15].

However, several disadvantages with the use of such nanocarbons do exist, especially in graphene-based CMCs, which are prone to anisotropy of electrical versus mechanical properties due to the preferential orientation of graphene flakes normal to the SPS uniaxial pressure direction. Moreover, carbonaceous materials are hydrophobic and are preferentially dispersed in non-polar organic solvents, whereas oxide ceramics are hydrophilic and are easily dispersed in water [20] to facilitate aqueous ceramic shaping processes. In general, these disadvantages mentioned hamper the applicability of CMCs based on nanocarbons [11,17,21].

Addressing the processing difficulties of carbon nanofiller-based ceramics, it has recently been shown that cellulose nanofibers (CNF) can be used as an excellent carbon precursor in ceramic matrices such as zirconia and alumina [22]. The strong hydrophilicity of CNF ensures facile and homogenous dispersion of the nanofibers in aqueous ceramic slurries [23,24]. A freeze-dried CNF-ceramic nanocomposite powder had been consolidated and SPS sintered. During the sintering process CNF was transformed within the ceramic matrix into a 3-dimensional (3D) network of few-layered graphene (FLG) sheets surrounding the grains and forming a highly homogeneous CMC framework structure. The ceramic was mechanically reinforced and percolation for electronic conduction was achieved with 0.5 wt% (2.1 vol%) CNF [23].

While cellulose is usually considered a non-graphitizable carbon precursor [24], cellulose nanofibers of high purity and crystallinity may indeed show propensity for graphitization [22,25]. However, the precise mechanism of the *in situ* graphitization process within CMCs has not been investigated so far and requires a more detailed study. For instance, the influence of the sintering conditions in terms of temperature, pres-sure and heating rate and the initial CNF content in the nanocomposite powder on the graphitization of CNF and the resulting properties of the ceramic material are yet to be elucidated. In this context, the tailoring of the charge transport properties including ionic and electronic conduc-tion of 8YSZ-carbon nanocomposites are of particular interest for a va-riety of sensor and energy applications [26]. For instance, the addition of carbon nanofillers such as carbon nanotubes and graphene to the 8YSZ matrix results in CMCs with mixed ionic-electronic conduction (MIEC) [16,17,27] suitable for high temperature electrochemical ap-plications in solid oxide fuel cells (SOFC) or sensors [28]. In particular, such CMCs may be an interesting alternative to SOFC anodes based on Ni/8YSZ cermets, which suffer from nickel coarsening and poor redox stability that can hamper both the electrical and mechanical properties [2].

In the present work, the influence of the CNF concentration and the SPS sintering temperature on the *in situ* transformation of CNF to graphite are investigated in detail, as well as the microstructural evolution of the matrix and the transport behavior of the resultant 8YSZ-graphite CMC. The initial CNF concentrations investigated were 0.75–2 wt% and the sintering temperatures ranged from 1200 °C to 1600 °C. Microstructural analysis revealed significant grain refinement when sintering at 1600 °C with 2 wt% CNF, while CNF was converted into turbostratic graphite. Concomitant electrical impedance spectroscopy (EIS) allowed separating the bulk and GB contributions to the dielectric properties and the analysis of their dependence on grain size and CNF concentration. Finally, the oxidation stability of the 8YSZ-2CNF CMC was evaluated in 5%H_2/Ar atmosphere up to 900 °C. It was found that the high electrical conductivity is maintained, which confirms suggests the possibility of this material to be used as an alternative anode electrode material in medium- to high-temperature SOFCs electrochemical devices.

2. Materials and methods

2.1. Materials and powder preparation

CNF was prepared by the TEMPO (2,2,6,6-tetramethylpiperidine 1-oxyl)-mediated oxidation method [29]. Prior to the TEMPO-mediated oxidation, 10 g of commercially bleached Eucalyptus globulus kraft pulp (kindly provided by La Montañanesa, Grupo Torraspapel, Zaragoza, Spain) were washed in 0.01 M HCl for demineralization. Next, the pulp was repeatedly washed with deionized water and resuspended in 1 L water. Subsequently, NaBr (0.1 g/g pulp), TEMPO (0.016 g/g pulp) and NaClO (6 mmol/g pulp) were added and the pH was kept at 10 by the addition of 1 M NaOH. The resulting suspension was constantly stirred for 4 h, and the pulp was filtered and washed. Cellulose nanofibers were eventually obtained by mechanical defibrillation of the TEMPO-oxidized pulp in a high-pressure microfluidizer M 110-P (Microfluidics Corp., USA) equipped with 100 μm and 200 μm interaction chambers, where the cellulose slurry was transformed into a transparent and highly viscoelastic gel of 1.5 wt% CNF concentration. The carboxylic charge density of CNF as a result of the TEMPO oxidation process was 890 μmol/g.

Commercial 8YSZ powder (TZ-8Y, Tosoh, Japan) was purchased in granulated form with a specific surface area of 16 m^2 g^{-1}. The powder was dispersed in water to form aqueous suspensions with 30 vol% of solid loading. Citric acid was used as a dispersant, where the pH of the suspensions was set to 8 using NH_4OH ammonium hydroxide. Aqueous CNF gel was admixed to attain nominal CNF concentrations of 0.75, 1 and 2 wt%. The suspensions were homogenized in a planetary ball mill using 3 mm ZrO_2 grinding balls at 300 rpm for 35 min. After a 1 min break the process was repeated in the opposite milling rotating direction. Then, the suspensions were quickly frozen in a liquid nitrogen bath and freeze-dried to obtain dry nanocomposite powder. The different compositions prepared were denoted as 8Y-*x*CNF with $x = 0$, 0.75, 1 and 2, where $x = 0$ corresponds to plain 8YSZ. A typical microstructure of the precursor nanocomposite powder can be seen in the Supplementary Material Fig. S1.

2.2. SPS sintering

The 8Y-CNF nanocomposite precursors were sintered in a SPS furnace (Dr. SINTER`S SPS-615E (Syntex Inc., Japan) using a 16 mm cylindrical graphite die. The inner side of the die was covered with a 0.5 mm graphite paper, whereas the outer side was covered with 5 mm thick graphite wool for insulation. Uniaxial contact pressure of 15 MPa (3 kN) was applied on the die containing the sample followed by evacuating the furnace chamber. A 100 °C/min heating ramp to reach the respective sintering temperatures of 1200, 1400 or 1600 °C was used, where the temperature of the die wall was measured using a pyrometer. After the set temperature was reached, the uniaxial pressure was increased to 80 MPa in a period of one minute, followed by a 5 min dwell time. After the end of sintering dwell time, the furnace was set to cool down to 1000 °C in 2, 4 and 6 min from 1200, 1400 and 1600 °C (100 °C/min). respectively. During these periods the pressure was gradually released to the value of contact pressure. Below 1000 °C furnace cooling was employed. Sintered samples are abbreviated as ^{8}Y–^{2}CNF-1400, for the 1400 °C sintered ^{8}Y–^{2}CNF composition.

2.3. Characterization of 8Y-CNF ceramic matrix composites

The densification behavior (dilatometry) during SPS was determined by simultaneous recording of the sintering temperature and the displacement of die punches as functions of sintering time, which are directly, although only roughly, reflecting the green body shrinkage as a result of the pressure-assisted SPS sintering. The final densities of the sintered samples were determined by the Archimedes method using distilled water as the immersion medium. The theoretical density was determined by the rule of mixtures, considering the amount of inserted CNF. The phase compositions were evaluated by X-ray diffraction (XRD) using a PANalytical X′pert PRO MPD diffractometer (PANalytical, Almelo, Netherlands) equipped with a PIXcel detector and using a Cu–K1 radiation source. The ceramic microstructure was analyzed on polished and thermally etched surfaces using a scanning electron microscope (SEM; Helios NanoLab 600i, FEI Europe B.V., Netherlands). Thermal etching (15 min) was performed at 1100 °C for samples sintered at 1200 °C, while samples sintered at 1400 °C and 1600 °C were thermally etched at 1300 °C. Average grain size and grain size distribution were determined by the linear intercept (no geometrical correction factor was employed) [30] and planimetric method, respectively, using ImageJ software.

For transmission electron microscopy (TEM) investigations, the samples were cut into cylinder shapes of 3 mm diameter using an ultrasonic cutter (Sonicut™ 380 Ultrasonic Cutter, SBT, USA). The TEM specimens were ground to a thickness of 100 μm and dimpled down to 15 μm at the disc center (Dimple grinder, Gatan Inc., Warrendale PA, USA), followed by ion-milling (PIPS, Precision Ion Polishing System, Gatan Inc., USA) using 3 kV Ar^+ ions at an incident angle of 8° until perforation. Detailed structural investigations of the sample were performed using a conventional 200 kV TEM (JEM-2100, Jeol Ltd., Tokyo, Japan) equipped with a LaB_6 electron source.

The carbon phase in the CMCs was characterized by Raman spectroscopy using a mSense-LabC1X Enwave Optronics Raman confocal microscope (Olympus) with a 532 nm excitation laser.

The mechanical properties were determined using a Vickers indentation testing device on polished surfaces. For each sample the hardness was evaluated from indents made with an applied load of 1 kgf with 10 s dwell time.

The dielectric properties of the sintered CMCs were characterized by electrical impedance spectroscopy (EIS), carried out on pellets sintered at 1200 ºC, 1400 ºC and 1600 ºC. The pellet surfaces were contacted with dc sputtered Au electrodes, which were covered with quick drying Ag paint. EIS measurements were taken between 160 and 560 K using a Novocontrol Alpha-A High Performance Frequency Analyzer equipped with a liquid nitrogen cooled sample chamber. EIS data was recorded between 1 Hz and 10 MHz in terms of the real and imaginary parts of the impedance ($Z' - Z''$) under steady state conditions, where each temperature was allowed to settle for 10 min before taking data using an 100 mV amplitude alternating voltage signal. The impedance $Z' - Z''$ data were converted into the notations of dielectric permittivity $\varepsilon' - \varepsilon''$ and modulus function $M' - M''$ using the standard conversions. An appropriate equivalent circuit model was employed to obtain a good fit of the data in all notations, which allowed determination of the bulk and grain boundary (GB) resistivity and dielectric permittivity separately.

Furthermore, the high-temperature stability against oxidation in reducing atmosphere was characterized by EIS analysis as well. In this case, Au paste electrodes were painted on the CMC pellets followed by annealing at 600 °C for 1 h in 5%H_2/Ar atmosphere. EIS measurements were carried out between RT and 900 ºC under isothermal conditions in reducing 5%H_2/Ar atmosphere, using a HP4284A precision LCR Meter in the frequency (f) range of 20 Hz – 2 MHz. All dielectric data were analyzed and fitted to the appropriate equivalent circuit models using commercial Zview® software. The data and fits were visualized by SSSS® custom built software.

3. Results and discussion

3.1. Sintering of 8Y-xCNF

Typical dilatometry curves for the SPS sintering process of 8Y-*x*CNF at 1600 °C are shown in Fig. 1a. The onset of densification occurred after 10 min of the SPS sintering process at ≈ 1000 °C. At the given initial (contact) pressure of 15 MPa the densification reached the maximum value possible under such pressure at temperatures of ≈ 1320 and 1370 °C. Note that the higher the amount of CNF in the sample the higher the first maximum in densification. This was regarded a first indication for the higher sintering driving force occurring when CNF was present in the 8YSZ matrix. With the increase in mechanical pressure to 80 MPa after 16 min of the SPS sintering process the densification further increased in all samples and complete densification was attained immediately or soon after the final sintering temperature was reached. Note that the addition of CNF again had a beneficial effect on promoting the densification completion as suggested by the sharper transition to the fully dense state, i.e., the flattening of the quasi-sigmoidal sintering curve that was also achieved earlier (inset in Fig. 1a).

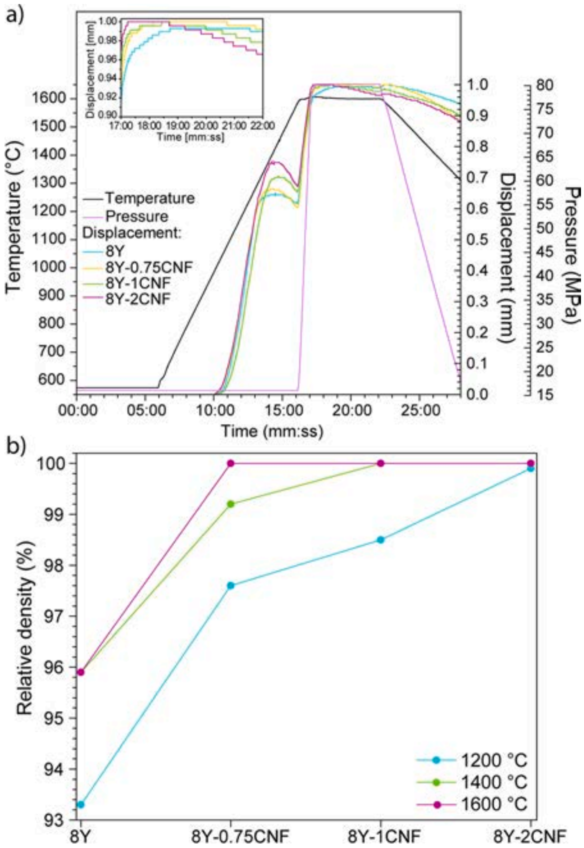

Fig. 1. Dilatometry curves for 8Y-*x*CNF showing the displacement and pressure of the graphite die as a function of SPS sintering time (a). The relative sintered densities of 8Y-*x*CNF as a function of the SPS sintering temperature and CNF content (b).

It can be stated that the addition of CNF had generally a marked benefit on the final density of the 8Y-*x*CNF CMCs. By applying 80 MPa (5 min dwell time), pure 8YSZ could not be SPS sintered to a denser state than 93 – 96% of the theoretical density (TD) (Fig. 1b) and the respective surface microstructure seemed to be at the threshold between closed and open porosity (see Section 3.2). However, when CNF was added the final density increased with the CNF concentration (Fig. 1b) and the necessary amount of CNF to attain full density (≈ 99% TD) decreased with the sintering temperature, i.e., 2 wt% CNF at 1200 °C, 1 wt% at 1400 °C and 0.75 wt% at 1600 °C.

3.2. Phase composition, microstructure and mechanical properties

XRD patterns of plain 8YSZ samples in Fig. 2a show that the cubic zirconia phase persisted for all three sintering temperatures. A clear broadening of the (111) reflection is observed for the 1200 °C sample indicative of a small crystallite size (Fig. 2b). As for sintered 8Y-*x*CNF samples, the cubic phase was again the only present phase (Fig. 2c), suggesting that the addition of CNF did not promote any obvious phase

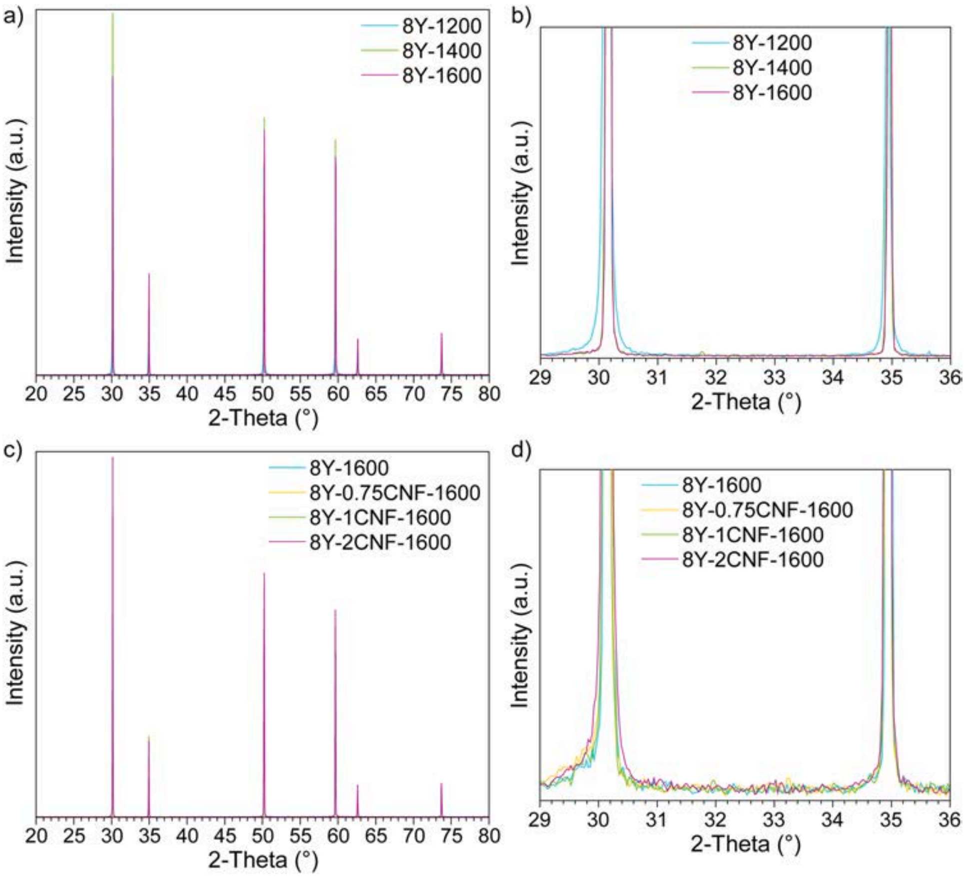

Fig. 2. XRD patterns of 8Y (a-b) and 8Y-*x*CNF (c-d) sintered at 1200, 1400 and 1600 °C, respectively.

partitioning in the ZrO_2-Y_2O_3 system [1,31]. The addition of CNF, however, affected the peak broadening at the highest sintering temperature of 1600 °C. The broadening was most pronounced with the addition of 2 wt% of CNF (Fig. 2d), which was again indicative of fine crystallinity and was regarded a sign of grain refinement within the 8YSZ matrix.

The microstructural evolution of the sintered samples is demonstrated in the SEM images in Fig. 3. The cumulative grain size distributions from the respective image analyses are displayed in Fig. 4 and the extracted d_{10}, d_{50} and d_{90} values are shown in Table S1 (Supplementary Material). The SEM images of the pure 8Y sintered samples show a clear tendency of grain growth with increasing sintering temperature. The d_{50} values increased from 0.18 to 1.60 and 4.92 μm for 1200, 1400 and 1600 °C, respectively. However, all pure 8Y samples contain substantial amount of remnant porosity (see also Fig. 1b), where the majority of the pores are located at the triple grain junctions (Fig. 3, first row). When CNF is introduced into the ceramic matrix a marked restriction in grain growth (Fig. 3) was observed, which was much more pronounced at higher sintering temperatures and CNF contents (Fig. 4, Table S1). According to the d_{50} values, the grain size was refined with the addition of 2 wt% CNF from an initial 0.18, 1.60 and 4.92 μm to 0.13, 0.31 and 0.52 μm for 1200, 1400 and 1600 °C sintering, respec-tively. The 5-fold and 10-fold reductions in d_{50} obtained at 1400 and 1600 °C, respectively, may be regarded as rather substantial. At the lowest sintering temperature of 1200 °C the refinement effect of added CNF is pronounced most likely due to the generally slower grain growth mechanism at low temperatures. It is known that 8YSZ has a high grain boundary mobility rate, especially when compared to 3 mol% yttria- stabilized tetragonal zirconia polycrystals (3Y-TZP), where the rate is in fact temperature dependent [12]. Therefore, specific strategies are required to limit grain growth while enabling complete densification.

The SEM images also reveal how the marked porosity in the sintered 8Y samples, observable as black spots at the triple junctions, is reduced with increasing CNF content. This observation is in agreement with the increased sintering density mentioned above (Fig. 1b).

The exact mechanism of the grain growth restriction by the CNF during the sintering process may in fact contain two factors. First, the pinning of grain boundaries to the CNF located along the GBs and, second, the blocking of atomic diffusion pathways across the GBs due to their full or almost full coverage by the CNF structure (see Fig. 8). The exact mechanism of improved densification sintering with the addition of CNF may be explained by the graphitization of CNF at higher sintering temperatures (see Section 3.3), where the resultant graphite may act as a lubricant and facilitate GB sliding, leading to enhanced densification and the observed higher final densities. This ability of graphene nano-structures to both hinder grain growth and ensure high densification of ceramic matrices has been demonstrated previously for SPS sintered ZrB_2 and TaC systems [32,33]. Herein, it was shown that the graphene nanoplatelets (GNPs) wrap around the grains acting as diffusion barriers and hindering grain growth, while GB sliding reduces the porosity.

The hardness (H_v) of the sintered 8Y-*x*CNF CMCs was analyzed by Vickers indentation (Fig. 5). It is known that in ceramics H_v correlates inversely with the grain size [34]. This is consistent with the hardness trend observed here in pure 8Y, where H_v decreases with increasing sintering temperature and the resultant increasing grain size (Table S1, Supplementary Material). Accordingly, H_v increases monotonously with CNF content in samples sintered at 1600 °C, to a lesser extent at 1400 °C, and at 1200 °C the hardness remains largely unchanged, corroborating the trends of the grain size with CNF addition mentioned above. For example, the grain size in 8Y-xCNF sintered at 1200 °C barely changes with the CNF content (Table S1), which correlates with the invariant hardness values. Contrarily, at 1600 °C the grain refinement is

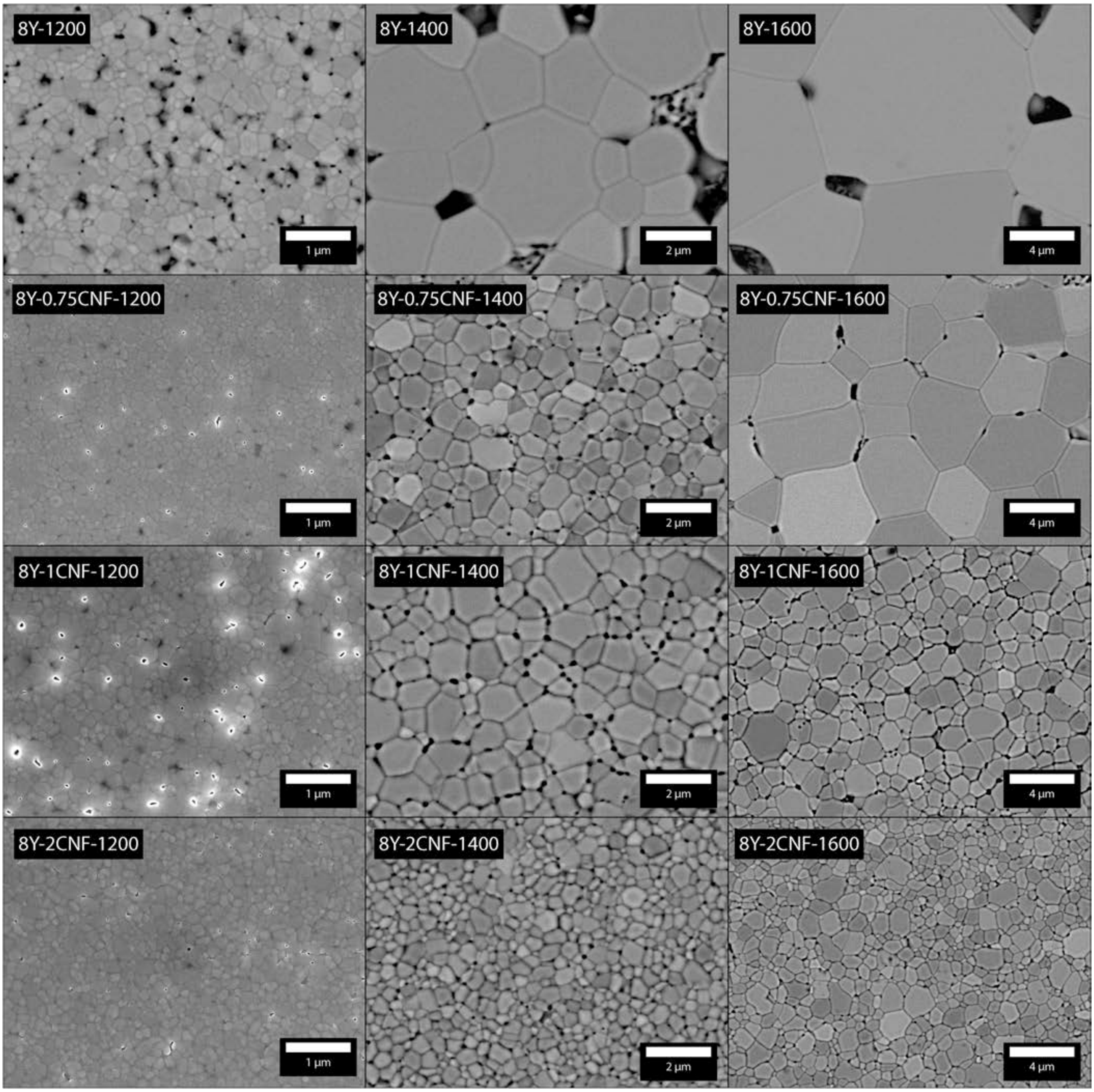

Fig. 3. SEM micrographs of sintered 8Y-*x*CNF samples (x = 0, 0.75, 1, 2) at 1200, 1400 and 1600 °C.

most pronounced, which corresponds with the marked increase in H_V. At 1400 °C the grain refinement is less significant, which correlates with the more moderate hardness gain with CNF addition observed.

3.3. *CNF graphitization during SPS*

The transformation of CNF within the 8YSZ matrix into graphitized carbon during sintering was investigated in detail by Raman spectroscopy. Fig. 6a shows the spectra of the samples sintered at 1200, 1400 and 1600 °C. At all three temperatures it can be observed that the Raman bands related to carbon, i.e. D ($\approx 1340\ \text{cm}^{-1}$), G ($\approx 1590\ \text{cm}^{-1}$) and 2D ($\approx 2695\ \text{cm}^{-1}$), emerge and increase in intensity as the CNF content increases from 0 to 2 wt%. At 0% CNF only the band originating from the cubic 8Y phase is detected ($610\ \text{cm}^{-1}$), which is in agreement with the XRD results. Upon addition of CNF, the D, G and 2D bands appear in the sintered materials, which are associated with sp^3 and sp^2 hybridized carbon and π-stacking interactions between graphene sheets, respectively. Therefore, these bands can be associated to defects in graphite (D), graphitic carbon (G) and the 3-dimensional ordering of graphite planes (2D), respectively [35]. Hence, the narrow and well-defined bands in the spectra suggest that nanocellulose was transformed into graphitic carbon during SPS sintering. Closer inspection of the data suggests that turbostratic graphite was formed, which will be discussed in more detail in the following:

1) The presence of the 2D band indicates that a graphitic material is present rather than graphene oxide or amorphous carbon [36],

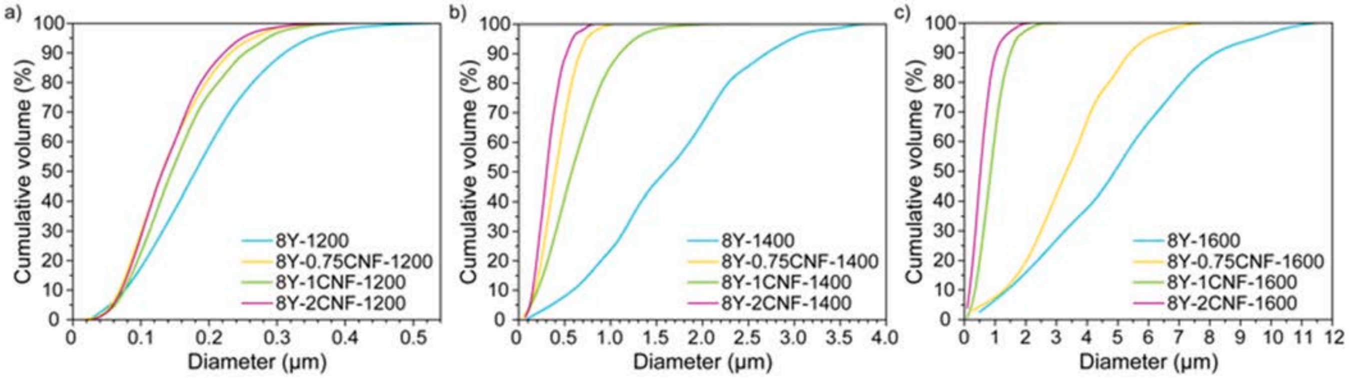

Fig. 4. Cumulative grain size distributions of 8Y-xCNF (x = 0, 0.75, 1, 2) sintered at 1200 °C (a), 1400 °C (b) and 1600 °C (c).

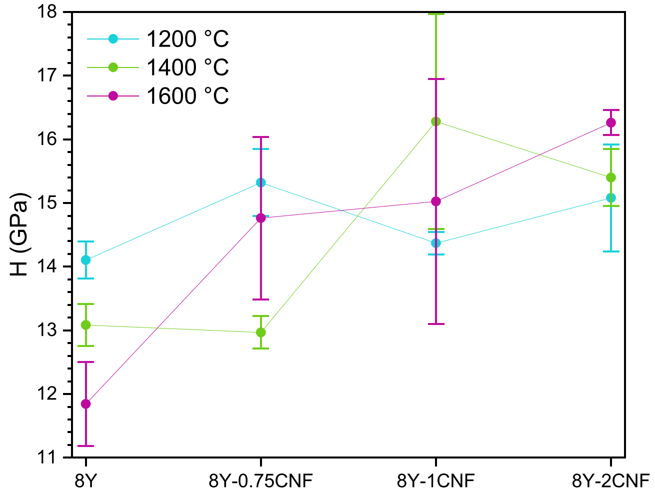

Fig. 5. Vickers hardness H_v of sintered 8Y-*x*CNF (x = 0, 0.75, 1, 2) samples.

which could both easily arise from the pyrolysis of an oxygen-rich carbohydrate [37–39].

2) The intensity of the G band is slightly higher or on par with the 2D band intensity ($I_G/I_{2D} \geq 1$) (Fig. 6b). This is indicative of graphitic carbon in contrast to single- or few-layered graphene that show a ratio $I_G/I_{2D} < 1$ [36]. This notion is corroborated by the fact that the D band is usually small or absent in graphene.
3) The 2D bands show a single peak profile, which is indicative of either graphene or turbostratic graphite [33]. As the former can be ruled out, it is suggested that turbostratic graphite was formed during SPS with rotational disorder of the graphene sheets along the *c*-axis (in an AB Bernal stacking).

Furthermore, the degree of graphitic organization, i.e. the lateral extent of sp^2 hybridized carbon crystallites, is generally expressed as the intensity ratio I_D/I_G of the corresponding Raman bands [40]. Since the lowest I_D/I_G ratio corresponds to the best graphitic organization, a clear preference of 1400 °C sintering can be deducted from Fig. 6c, as well as a preference of low CNF concentrations. According to the Tuinstra-Koenig (TK) relation, the I_D/I_G ratio scales inversely with the graphite crystallite size above 2 nm [41,42]. In the present case, the lowest I_D/I_G ratios are between 0.68 and 0.91, which corresponds to 20–28 nm crystallite size according to the generalized, energy-dispersive TK equation:

$$L_a = \frac{560}{E_l^4}\left(\frac{I_D}{I_G}\right)^{-1} \tag{1}$$

where L_a is the crystallite size and E_l is the laser energy (2.33 eV) [43,44].

These relatively large crystallite sizes also correspond well with the narrow G and 2D bands (FWHM of 43 and 77 cm^{-1}, respectively), which are indicative of crystalline graphite. Carbonaceous materials from biomass usually show higher FWHM values of 100–200 cm^{-1} and the 2D band often appears only as a “broad bump” [45]. Interestingly, the FWHM values of all three D, G and 2D bands slightly increase with increasing CNF concentration (see Table S2 in Supplementary Material). Hence, the formation of well-organized graphite planes possibly pro-ceeds more efficiently at lower cellulose concentrations, whereas higher concentrations lead to more defects. This observation is also supported by the I_G/I_{2D} ratio being slightly below 1 for 0.75% CNF, which indicates few-layered graphene rather than 3D graphite crystallites for this composition [46]. However, the optimum 0.75% CNF concentration is below the percolation threshold for electronic charge transport of ≈ 1.1–1.5% (see Section 3.4) and is, thus, less relevant for applications where MIEC is desired.

On the other hand, a number of defect-activated bands are visible at 1605 cm^{-1}, 2460 cm^{-1}, 2935 cm^{-1} and 3240 cm^{-1} in deconvoluted spectra (Fig. S2, Supplementary Material), which are assigned to the Raman modes D′, G* , D+D′ and 2D’, respectively [36]. These bands can be attributed to crystallite edge and point defects (vacancies, hetero-atoms) in the graphitic sheets [47,48]. Thus, it can be assumed that the turbostractic graphite sheets display a certain amount of 0D and 1D defects in addition to *c*-axis disorder. On the other hand, the relatively narrow D band with a FWHM of 46 cm^{-1} suggests that the amount of sp^3 carbon related to functional groups (carbon-heteroatom bonds) is rather small considering the carbohydrate origin of this graphitic material.

The apparent graphitization of CNF during SPS may be explained as follows. Typically, the graphitization of biomass proceeds from a dehydration step (100–300 °C) over a carbonization step (300–900 °C) to a graphitization process at 2400–3000 °C in vacuum [50]. Although carbon derived from cellulose is widely regarded as non-graphitizable, there are several reports on specific conditions, where cellulose *can* be graphitized. It was observed that a combination of tensile stress and nanoscale dimensions of the cellulose source favors graphitization in conventional furnaces at 2200–3000 °C [25,49]. While the former stretches the carbonized fibers and aligns the growing graphite crystallites, the latter ensures high specific surface area, high degree of nanofiber dispersion and high cellulose crystallinity in sources like bacterial cellulose, tunicate cellulose and electrospun regenerated cellulose nanofibers [50–52]. The nanoscale dimensions may in fact be crucial, because the graphitization of the ex-cellulose carbon fibers proceeds from the surface into the bulk [25]. Hence, a nanofiber is readily graphitized in contrast to thicker and aggregated micron-sized fibers, even at relative low temperatures of 1500 °C [52]. The diameter of the CNF used in this work is 2–3 nm as previously determined by AFM [22], which is 1–2 orders of magnitude smaller than the dimensions reported in the literature for graphitizable cellulose sources [50–52]. On the other hand, the necessary tensile stress is usually

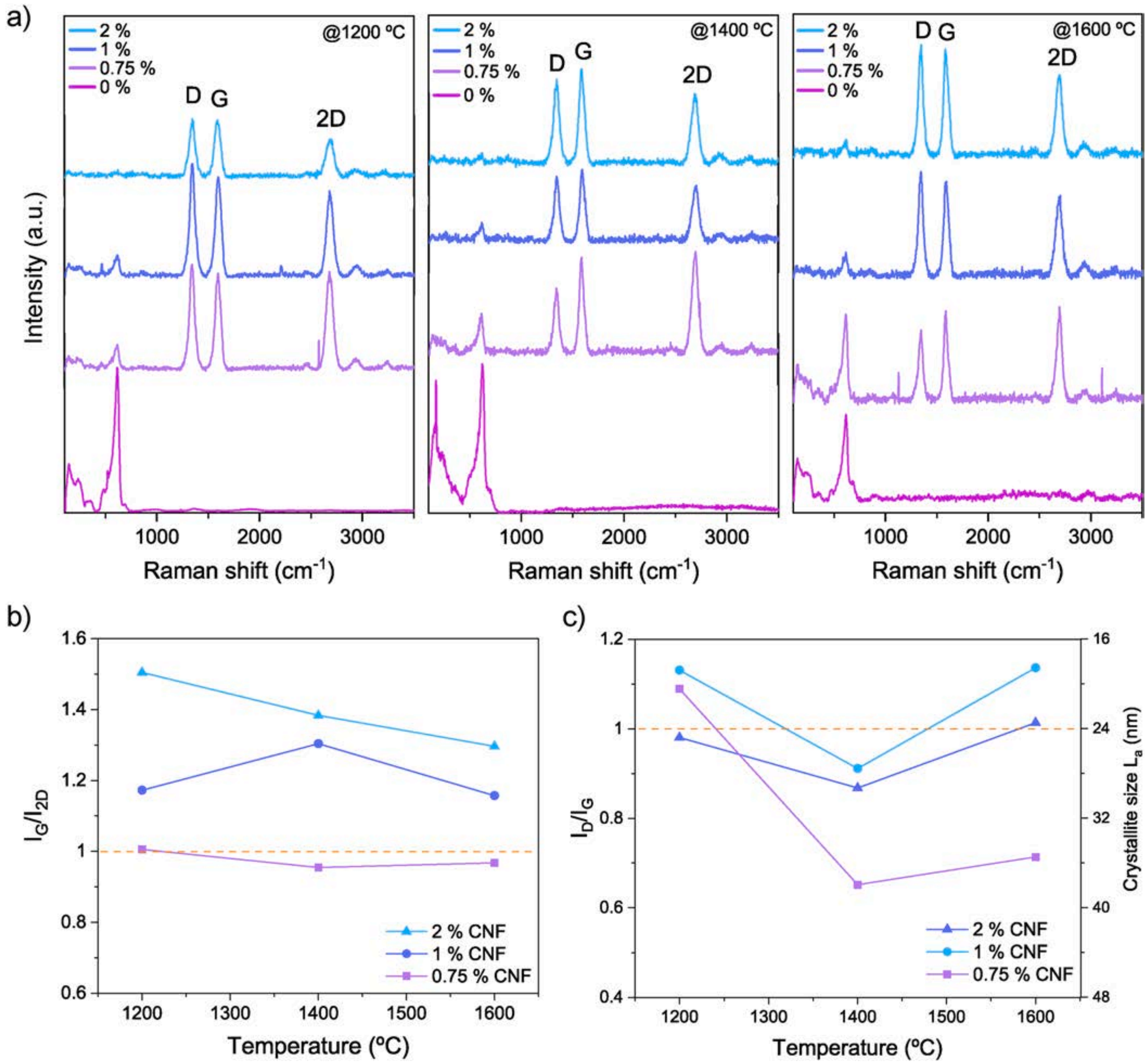

Fig. 6. Raman spectra of 8Y-*x*CNF ($x = 0$, 0.75, 1, 2) sintered at 1200, 1400 and 1600 °C, respectively (a). Intensity ratio of the G and 2D bands (b) and the intensity ratio of the D and G bands as well as the L_a crystallite size calculated from Eq. (1) (c) as function of the sintering temperature and CNF content.

applied to fibers in the process of carbon fiber production [49]. Here, uni-axial mechanical pressure of 80 MPa is applied to the samples during SPS, resulting in multiple stress regimes among the ceramic particles that are wrapped with cellulose nanofibers. During such densification, tensile, compressive and shear stresses act on the densifying ceramic matrix originating from grain sliding and rotation. As a consequence, large stresses are exerted on the ex-CNF carbon fibers, leading to a reorganization into graphitic sheets (see Fig. 8). This proposed mecha-nism is supported by sintering experiments in a conventional, pres-sureless vacuum furnace, where no graphite bands were observed in the Raman spectra (Fig. S3, Supplementary Material). As shown above, lower I_G/I_{2D} and I_D/I_G ratios were observed for samples with low CNF concentration, which may be understood as follows. At low CNF con-centrations the nanofibers within the ceramic matrix may be more dispersed and the tensile stress between the sliding grains acts on fewer nanofibers, which may render the process more efficient. Hence, thin graphite is formed with large (15–30 nm) lateral crystallite dimensions.

This is confirmed by TEM investigations showing 6 nm thick

Fig. 7. TEM micrograph of ex-CNF graphite sheets between 8YSZ grains in 8Y–2CNF-1600.

graphitic layers consisting of approximately 10 graphene layers (Fig. 7). On the left-hand side of the TEM micrograph, two thin strands are visible that merge into a single, thicker layer of ≈ 10 nm thickness that enters into a triple grain junction. It can be seen that at this triple grain junc-tion, the original CNF was piled, instead of being stretched and stressed as is the case in between two grains. As a consequence, the micro-structure of the formed carbonaceous phase lacks clear ordering and layering.

The two-fold processes during SPS sintering of 8Y-CNF are illustrated in Fig. 8. The grain sliding and rotation results in microstructural refinement, where CNF blocked diffusion pathways along GBs. In addition, the SPS uniaxial pressure creates localized stresses that likely contribute to the graphitization of CNF leading to intergranular tur-bostratic graphite.

3.4. Dielectric properties

Impedance spectroscopy data from pellets sintered at the optimum graphitization temperature of 1400 °C with 0%, 0.75% and 1% CNF are shown in Figs. 9 and 10. Fig. 9a-c show the data plotted in the format of the complex impedance plots of imaginary part of the impedance Z'' vs the real part Z'. The data show typical signs of two slightly overlapping semicircles that can be attributed to the dielectric response from the bulk and the GB areas. Furthermore, the typical low frequency pike structure indicates a blocking CMC/electrode interface (IF), which sig-nals macroscopic ionic type charge transport below the threshold for percolating electronic conduction. For higher initial CNF percentages (e.g. 2 wt% CNF), macroscopic metallic type conduction was dominant

(data not shown here). In this case, the technique of impedance spectroscopy is no longer useful, because bulk, GB and IF contributions can no longer be separated and only the direct current (DC) resistivity is accessible. The CNF percolation threshold must be therefore higher than 1 wt% but lower than 2 wt%. In a previous study, using a 3YSZ ceramic matrix, it was found that the percolation threshold was between 0.5 and 1 wt% CNF concentration [22]. Therefore, it was hypothesized that the percolation threshold in the present study (using 8YSZ) should be ob-tained with the addition of 1 wt% CNF, but certainly not exceeding 1.5 wt% CNF. This was corroborated by the dielectric data discussed further below. It was shown that the actual ex-CNF graphite content in the ceramic matrix is about 50% lower than the initial CNF content, mainly due to thermal decomposition during SPS [22]. Hence, the graphite percolation threshold in the CMCs investigated here may be as low as ≈ 0.6–0.75 wt% (or ≈ 1.6–2.0 vol% graphite). This value is lower than those reported for GNP/8YSZ (7.1 vol%) [17] and FLG/3YSZ (2.5 vol%) [21].

The diameter of the bulk and GB semicircles shown in Fig. 9a-c correspond to the bulk and GB resistivities [54–56]. This notion allows a quick analysis of the trends of bulk and GB resistivity with CNF content. It can be seen that the overall resistivity (bulk + GB) at 560 K decreases with increasing CNF content, which is the equivalent trend observed at all other temperatures. This can be interpreted as a short-circuiting of an increasing amount of 8YSZ grains with an increasing content of highly conducting ex-CNF graphite, which may act as an internal electrode within the ceramic.

In addition, a change in the ratio between bulk and GB resistivity was observed (Fig. 9a-c). The GB resistivity seems to amount to a higher percentage of the overall response with increasing CNF doping (Fig. 10). This may be associated to two main factors:

(i) The grain size refinement brought about by increasing CNF content leads to a larger number of GBs present in the CMCs and, concomitantly, to a proportionally higher GB resistivity as compared to the bulk.

(ii) The CNF may be accumulating at the GB areas and thus, blocking the pathways for ionic conduction across and/or along the grain boundaries, which was suggested previously for GNP/8YSZ [17].

It can be seen from Fig. 9b-c that the overall ionic resistivity (bulk + GB) drops drastically for the 8Y–1CNF sample by almost an order of magnitude as compared to the 8Y-0.75CNF sample. This corroborates the notion that the 8Y–1CNF sample may in fact be very close to the percolation threshold, possibly in the range of ≈ 1.1 – 1.2 wt% initial CNF (or 4.6 – 5.0 vol% CNF).

Each of the data sets had been fitted with an equivalent circuit model based on series RC elements, where the model is presented in the insets of Fig. 9a-c. Each RC element represents one dielectric contribution (bulk and GB contributions, whereas the contribution from the blocking IF was not reflected in the equivalent circuit models, since it has not the regular semicircular shape that can be modelled with RC elements. The ideal capacitor used in the RC elements had to be replaced by a non-ideal constant-phase element (CPE) to obtain good fits. On a microscopic basis, the CPE is commonly interpreted as a reflection of a broadening of the distribution of relaxation times τ ($\tau = R \times C$) across the ceramic. Good agreement between data and model was obtained.

In addition to the standard and expected bulk, GB and IF contributions, the conducting graphite phase is reflected in the dielectric data plotted in the format of Z' vs f (Fig. 9d-f) at 220 K in terms of a slight upturn or plateau. The graphite phase can be identified best for the sample containing 1 wt% CNF, whereas for lower CNF concentrations the plateau gradually vanishes as expected. In fact, the graphite phase

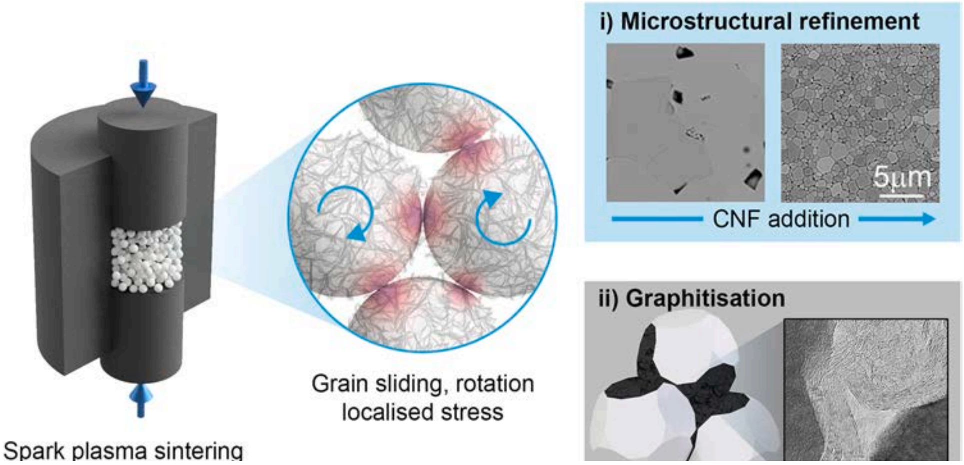

Fig. 8. Illustration of microstructural refinement and *in situ* graphitization during SPS sintering of 8YSZ grains surrounded by CNF.

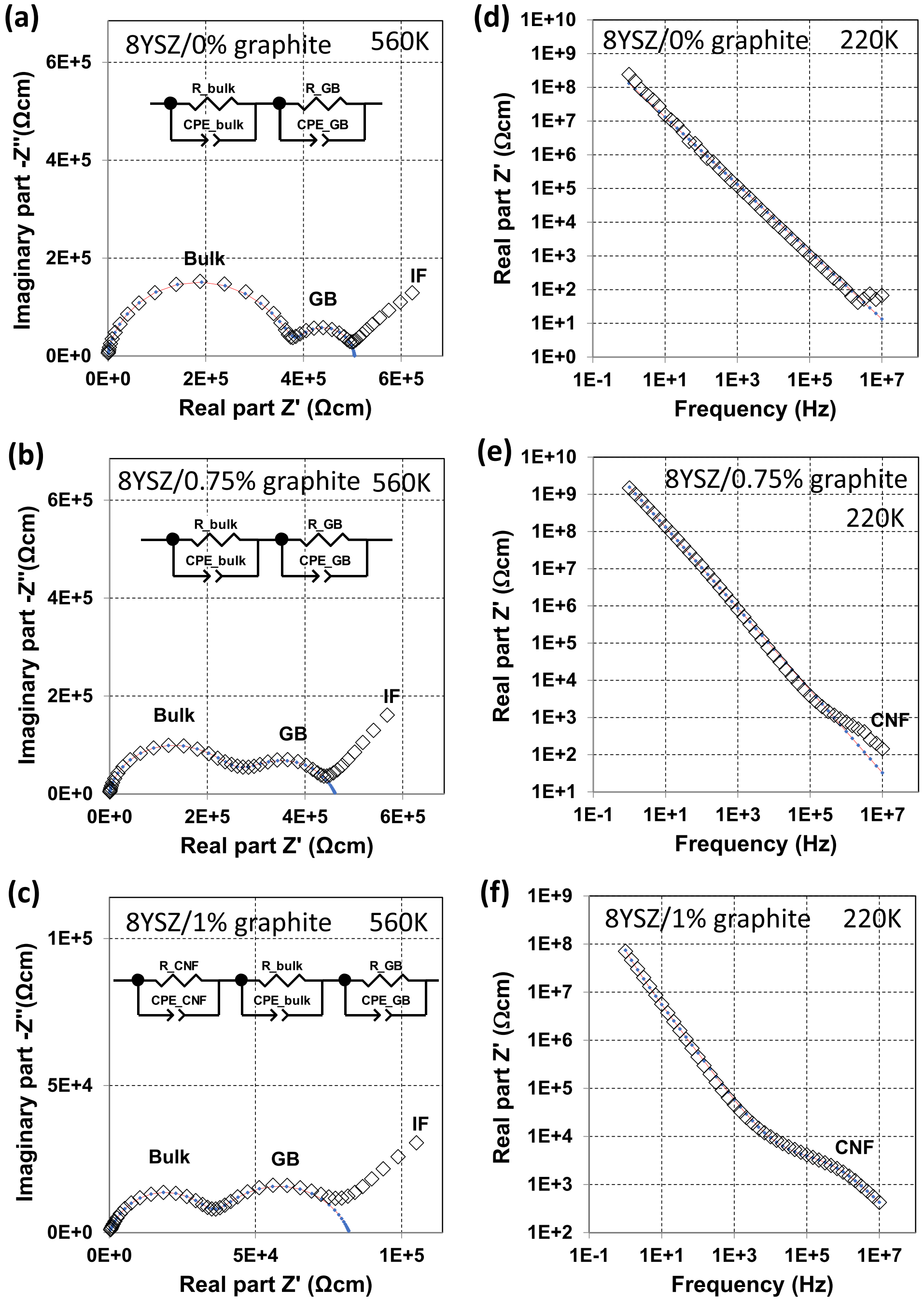

Fig. 9. Dielectric data from 8Y-*x*CNF with x = 0, 0.75, 1 sintered at 1400 °C. *Z*'' vs *Z*' plots at 560 K (a-c) and *Z*' vs *f* plots at 220 K (d-f). Open symbols correspond to the data, solid squares and lines to the fits using the equivalent circuits in the (a-c) figure insets.

had been detected previously in a 3YSZ/0.5%CNF sample as an additional dielectric contribution [21], but is much better visible here in the 8Y–1CNF-1400 sample. The visibility and spectral weight are in fact good enough here to allow fitting it with an additional RC or R-CPE element in series (see Fig. 9c inset), which was not possible in the samples investigated in reference [22] and in the 8Y-0.75CNF-1400 sample here in this study. This confirms again that the 1 wt% CNF sample in the present work may be very close to the percolation threshold. It is worth noting at this point that the YSZ doping level seems to affect the percolation threshold. In 3YSZ-1%CNF, percolation and metallic conduction had been detected, whereas the 8YSZ-1%CNF sample used here is very close but below the percolation threshold.

Manifestations of the graphite phase can also be found by plotting the data in the format of the real part of the dielectric permittivity *ε*' vs *f* (Figs. S4a-c, Supplementary Material).

Figs. S4d,e (Supplementary Material) and Fig. 11 show the trends of the bulk, GB and CNF resistivity, which were obtained by fitting the dielectric data to the equivalent circuit models displayed in Fig. 9a-c.

Fig. 11 shows the logarithmic resistance of the graphite phase plotted vs 1/T for the 1% CNF sample. It can be seen that a linear fit through the data yields an activation energy of 0.05 eV, in a similar range like pre-viously reported values [22].

3.5. *High-temperature oxidation stability*

The stability against oxidation in a reducing atmosphere at medium to high temperatures (500–900 °C) was studied on the sintered sample 8Y–2CNF-1400 to evaluate the viability of this material for its potential

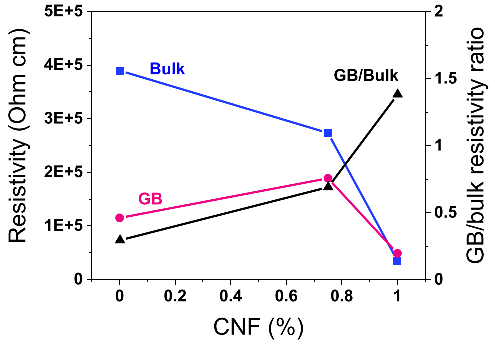

Fig. 10. Bulk and GB resistivity at 560 K and their ratio as a function of the initial CNT content in sintered 8Y-*x*CNF-1400.

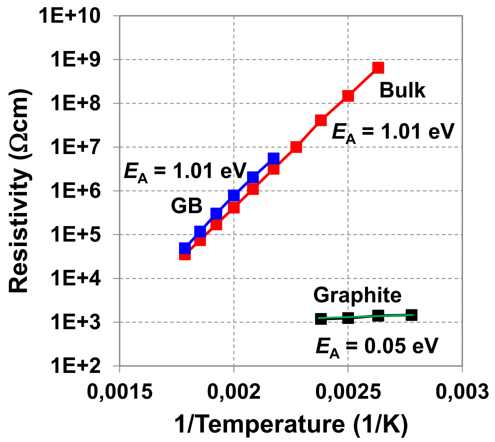

Fig. 11. Resistivity values of 8Y–1CNF-1400 obtained from the bulk and GB resistors in the equivalent circuit models plotted on logarithmic axes vs 1/*T*. The respective charge transport activation energies are indicated.

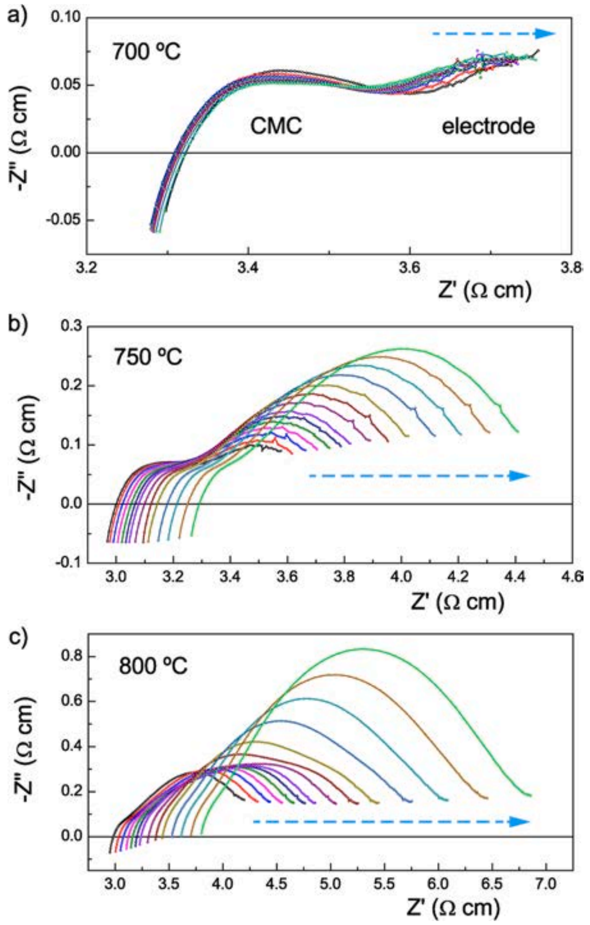

Fig. 12. Complex impedance plots of sintered sample 8Y–2CNF-1400 under isothermal conditions at 700 C (a), 750 °C (b) and 800 °C (c) in 5%H_2/Ar atmosphere. Dashed arrows indicate plots at increasing time (0, 1, 2, 3, 4, 5, 6, 8, 10, 12, 15, 18, 21, 24 h).

use as anode in SOFCs. This sample showed percolation of the ex-CNF graphite phase and metallic-type conduction at low temperature. EIS measurements were conducted in reducing 5%H_2/Ar atmosphere ($p_{O2} \approx 10^{-5}$ atm) at increasing temperatures to study the evolution over time of the total *dc* conductivity (σ_{dc}) under isothermal conditions (Fig. 12). It should be mentioned that under air atmosphere ($p_{O2} \approx 0.21$ atm), σ_{dc} decreases by several orders of magnitude at 500 °C, due to the fast oxidation of the ex-CNF graphite phase [17].

Under 5%H_2/Ar atmosphere, no significant changes over time in σ_{dc} or the complex impedance plots were observed up to 700 °C (Fig. 12a), demonstrating good resistance of the ex-CNF graphite phase to degra-dation in reducing atmosphere up to this temperature. Similar obser-vations were also made for 8YSZ/reduced graphene oxide [57] and for 8YSZ/graphene [17]. At 750 °C, the impedance response started to evolve over time and more than one semicircle is visible in the complex impedance plots (Fig. 12b). Note that the ex-CNF graphite phase in this sample acts as an internal electrode at the GBs, short-circuiting the grains. Hence, the main contribution to the impedance response comes from percolating electronic conduction pathways through the ex-CNF graphite phase at the GBs (high-frequency data), whose associated impedance value changes from 3.35 to 3.5 Ω cm (less than 5%) during 24 h at 750 °C. The low-frequency semicircles with increasing imped-ance from 0.25 to 1.0 Ω cm during 24 h are likely to be related with the degradation of the CMC/electrode interface.

A similar evolution over time was observed at 800 °C (Fig. 12c), where more than two semicircles are clearly visible. In this case, impedance values associated to electronic conduction of the ex-CNF graphite phase at GBs increase from 3.0 to 4.0 Ω cm (about 25%) dur-ing 24 h, while the rest might come from degradation of the ceramic/electrode interface. In both cases, oxidation of the ex-CNF graphite phase might account for the observed decrease in conductivity over time above 750 °C, most probably by chemical reactions at the interfaces with residual oxygen in the atmosphere, though reaction with oxygen from the 8YSZ structure in the bulk cannot be ruled out [17]. Indeed, the ex-CNF graphite phase at the GBs might be blocking the oxygen-ion diffusion between 8YSZ grains (*vide supra*).

The 8Y–2CNF-1400 sample was finally annealed at 900 °C for 24 h in 5%H_2/Ar atmosphere and new electrodes were painted, and the effects of degradation of the ceramic/electrode interfaces can be ruled out in this way. Fig. 13a shows the temperature evolution of σ_{dc} from RT to 900

C, calculated from EIS plots using an equivalent circuit model based on

series R-CPE elements. Measurements before and after annealing (the latter with new electrodes) are given, and several points are worth to be highlighted. Firstly, the high conductivity above 0.1 S cm^{-1} in the medium to high temperature range (500–900 °C) suggests that these CMCs are suitable for intermediate- and high-temperature electrochemical devices. It should be noted that σ_{dc} by EIS analysis is lower than that expected by measuring in a 4-electrode geometry [22]. Note also the very low $E_A \approx 0.02$ eV at low temperature in both runs, which confirms that the prevailing conduction mechanism is of electronic origin in this temperature range.

Secondly, Fig. 13a also reveals that some oxidation of the ex-CNF graphite phase takes place during high-temperature annealing, in addition to degradation of the ceramic/electrode interfaces, so σ_{dc} decreases to half the initial value in the second run. Nevertheless, σ_{dc} values are still very high (0.17 S cm^{-1} at 900 °C), one order of

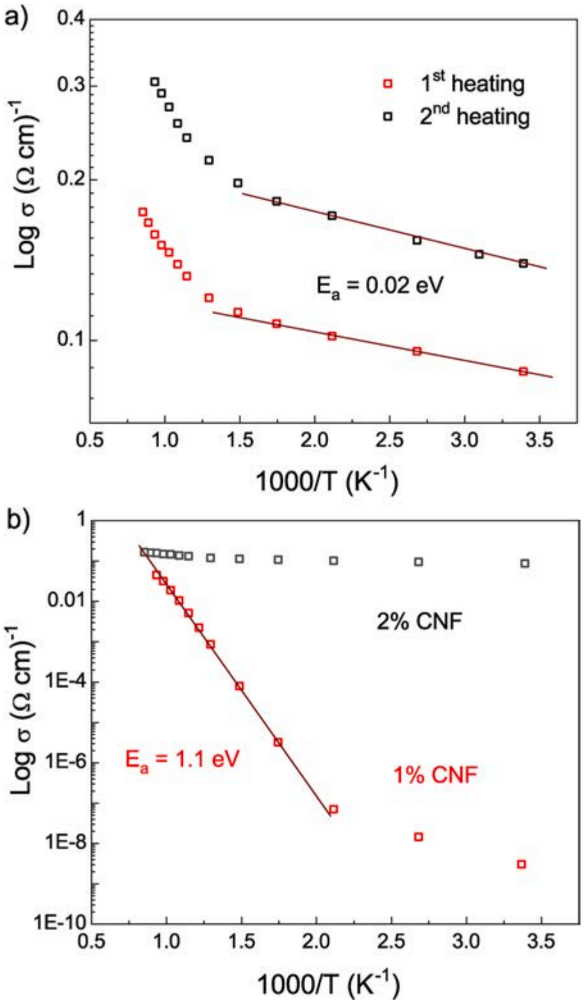

Fig. 13. *dc* conductivity (σ_{dc}) versus inverse absolute temperature of (a) 8Y–2CNF-1400 during first and second heating runs, that is, before and after annealing at 900 °C/ 24 h in 5%H_2/Ar atmosphere, respectively, and (b) comparison with 8Y–1CNF-1400 °C in 5%H_2/Ar atmosphere.

magnitude higher than, for instance, in GNP/8YSZ [17]. This underscores the good performance of these CMCs in 5%H_2/Ar atmosphere up to 900 °C.

Finally, the slope of the curves is changing at high temperature, which is reversibly observed in the heating/cooling cycles. Thus, it cannot be related to any evolution over time caused by degradation. This increase of conductivity at high temperature seems to be related to the appearance of another conduction mechanism, most probably due to the ionic conduction of the 8YSZ structure that starts to contribute increasingly at increasing temperature [58]. This confirms that mixed ionic/electronic conduction may occur over a wide temperature range (500–900 °C) in sample 8Y–2CNF-1400, and intermediate- and high-temperature electrochemical applications would be feasible [59,60].

Fig. 13b shows the σ_{dc} curves up to 800 °C for sample 8Y–1CNF-1400 along with data for sample 8Y–2CNF-1400, for the sake of comparison. The former was shown to be below the percolation threshold, so that ionic conduction dominates the total impedance response, as is denoted by its E_A value close to 1.1 eV. It can be observed that conductivity values for this sample approach those of sample 8Y–2CNF-1400 at higher temperature, suggesting that the increase in conductivity at high temperature in the latter (Fig. 13a) is indeed related to the increasing contribution of ionic conduction in the high temperature range.

4. Conclusions

Nanocellulose was shown to have a dual function in the preparation of dense and electro-conducting CMCs. Firstly, it ensured microstructural grain refinement with d_{50} values between 130 and 520 nm depending on the SPS sintering temperature and CNF content. The refinement effect was most apparent at 1600 °C. The good miscibility of the CNF gel with the 8YSZ slurry together with the nanoscale dimensions and flexibility of CNF ensures the formation of a uniform fiber-grain network, which allows for grain sliding and grain boundary pinning as primary densification and grain refinement mechanisms. Secondly, the graphitization of nanocellulose imparts electrical conductivity to the CMC by producing thin, turbostratic graphite layers within the 8YSZ matrix related to the original nanoscopic dimensions of CNF. Therefore, the percolation threshold around ≈ 1.6 vol% graphite for electrical conduction is rather low compared with other ceramic-graphite/graphene composites. Importantly, the CMCs showed MIEC behavior that is stable over a wide temperature range (500–900 °C) with high conductivity values. The latter is key in high-temperature electrochemical applications like solid oxide fuel cells, where 8YSZ-CNF ~~may~~ might be an interesting alternative to Ni/YSZ cermets as an anode material after overcoming important roadblocks like oxidation stability under wet fuel conditions, possible reoxidation, generation of a porous microstructure and clarification of the catalytic activity and diffusion pathways.

Acknowledgements

PH thanks the JECS Trust for funding a mobility stay project in 2020 (Contract 2019231). The Slovenian Research Agency is acknowledged for funding through research program P2-0087. RS acknowledges funding from the EU FLAG-ERA project To2Dox (JTC-2019-009) and the Spanish MINECO (Grant PID2020-118078RB-I00). Financial support from the Agencia Estatal de Investigación (AEI, Spain) and the FEDER Program (EU) is acknowledged (MAT2015-71117-R). BW thanks the MICINN for a JIN contract (PID2019-107022RJ-I00). HA thanks the MICINN for funding through project MAT2017-88788-R.

References

[1] D.M. Lipkin, J. a Krogstad, Y. Gao, C. a Johnson, W. a Nelson, C.G. Levi, Phase evolution upon aging of air-plasma sprayed t ′-zirconia coatings: I-synchrotron x-ray diffraction, J. Am. Ceram. Soc. 96 (2013) 290–298, https://doi.org/10.1111/j.1551-2916.2012.05451.x.

[2] B. Shri Prakash, S. Senthil Kumar, S.T. Aruna, Properties and development of Ni/YSZ as an anode material in solid oxide fuel cell: a review, Renew. Sustain. Energy Rev. 36 (2014) 149–179, https://doi.org/10.1016/j.rser.2014.04.043.

[3] X.Y. Tai, A. Zhakeyev, H. Wang, K. Jiao, H. Zhang, J. Xuan, Accelerating fuel cell development with additive manufacturing technologies: state of the art, opportunities and challenges, Fuel Cells (2019) 1–15, https://doi.org/10.1002/fuce.201900164.

[4] J. Jian, A. Chang, B. Yang, Y. Zhang, Electrical property of 8-mol% yttria-stabilized zirconia electrolyte by spark-plasma sintering, Sci. China Ser. E Technol. Sci. 47 (2004) 569–576, https://doi.org/10.1360/04ye0074.

[5] K. Rajeswari, M.B. Suresh, D. Chakravarty, D. Das, R. Johnson, Effect of nano-grain size on the ionic conductivity of spark plasma sintered 8YSZ electrolyte, Int. J. Hydrog. Energy 37 (2012) 511–517, https://doi.org/10.1016/j.ijhydene.2011.09.018.

[6] P. Mondal, A. Klein, W. Jaegermann, H. Hahn, Enhanced specific grain boundary conductivity in nanocrystalline Y2O3-stabilized zirconia, Solid State Ion. 311 (1999) 331–339.

[7] C.M. Fernandes, A. Castela, F.M. Figueiredo, J.R. Frade, Microstructure-property relations in composite yttria-substituted zirconia solid electrolytes, Solid State Ion. 193 (2011) 52–59, https://doi.org/10.1016/j.ssi.2011.02.017.

[8] H.-S. Yang, G.-R. Bai, L.J. Thompson, J. a Eastman, Interfacial thermal resistance in nanocrystalline yttria-stabilized zirconia, Acta Mater. 50 (2002) 2309–2317, https://doi.org/10.1016/S1359-6454(02)00057-5.

[9] T. Takeuchi, I. Kondoh, N. Tamari, N. Balakrishnan, K. Nomura, H. Kageyama, Y. Takeda, Improvement of mechanical strength of 8 mol% Yttria-stabilized zirconia ceramics by spark-plasma sintering, J. Electrochem. Soc. 149 (2002) A455, https://doi.org/10.1149/1.1456915.

[10] M. Estili, A. Kawasaki, Y. Sakka, Highly concentrated 3D macrostructure of individual carbon nanotubes in a ceramic environment, Adv. Mater. 24 (2012) 4322–4326, https://doi.org/10.1002/adma.201201134.

[11] B. Rom´an-manso, E. Domingues, F.M. Figueiredo, M. Belmonte, P. Miranzo, Enhanced electrical conductivity of silicon carbide ceramics by addition of graphene nanoplatelets, J. Eur. Ceram. Soc. 35 (2015) 2723–2731, https://doi.org/10.1016/j.jeurceramsoc.2015.03.044.

[12] S. Schwarz, O. Guillon, Two step sintering of cubic yttria stabilized zirconia using field assisted sintering technique/spark plasma sintering, J. Eur. Ceram. Soc. 33 (2013) 637–641, https://doi.org/10.1016/j.jeurceramsoc.2012.10.002.

[13] M. Mazaheri, A.M. Zahedi, M.M. Hejazi, Processing of nanocrystalline 8 mol% yttria-stabilized zirconia by conventional, microwave-assisted and two-step sintering, Mater. Sci. Eng. A 492 (2008) 261–267, https://doi.org/10.1016/j.msea.2008.03.023.

[14] J. Langer, M.J. Hoffmann, O. Guillon, Electric field-assisted sintering in comparison with the hot pressing of yttria-stabilized zirconia, J. Am. Ceram. Soc. 94 (2011) 24–31, https://doi.org/10.1111/j.1551-2916.2010.04016.x.

[15] A.M. Zahedi, J. Gonzalez-Julian, M. Mazaheri, J. Javadpour, H.R. Rezaie, O. Guillon, Field-assisted/spark plasma sintering behavior of CNT-reinforced zirconia composites: a comparative study between model and experiments, J. Eur. Ceram. Soc. 35 (2015) 4241–4249, https://doi.org/10.1016/j.jeurceramsoc.2015.07.030.

[16] A. Rinc´on, R. Moreno, C.F. Guti´errez-Gonz´alez, R. Sainz, M.D. Salvador, A. Borrell, Colloidal processing of fully stabilized zirconia laminates comprising graphene oxide-enriched layers, J. Eur. Ceram. Soc. 36 (2016) 1797–1804, https://doi.org/10.1016/j.jeurceramsoc.2016.01.035.

[17] D. Marinha, M. Belmonte, Mixed-ionic and electronic conduction and stability of YSZ-graphene composites, J. Eur. Ceram. Soc. 39 (2019) 389–395, https://doi.org/10.1016/j.jeurceramsoc.2018.09.016.

[18] S.-W. Kim, S.-J.L. Kang, I.-W. Chen, Electro-sintering of Yttria-stabilized cubic zirconia, J. Am. Ceram. Soc. 96 (2013) 1398–1406, https://doi.org/10.1111/jace.12291.

[19] R. Chaim, G. Chevallier, A. Weibel, C. Estourn`es, Grain growth during spark plasma and flash sintering of ceramic nanoparticles: a review, J. Mater. Sci. 53 (2018) 3087–3105, https://doi.org/10.1007/s10853-017-1761-7.

[20] A. Centeno, V.G. Rocha, B. Alonso, A. Fern´andez, C.F. Gutierrez-gonzalez, R. Torrecillas, A. Zurutuza, Graphene for tough and electroconductive alumina ceramics, J. Eur. Ceram. Soc. 33 (2013) 3201–3210, https://doi.org/10.1016/j.jeurceramsoc.2013.07.007.

[21] C. Mu˜noz-Ferreiro, C. L´opez-Pernía, ´A. Gallardo-L´opez, R. Poyato, Unravelling the optimization of few-layer graphene crystallinity and electrical conductivity in ceramic composites by Raman spectroscopy, J. Eur. Ceram. Soc. 41 (2021) 290–298, https://doi.org/10.1016/j.jeurceramsoc.2021.09.025.

[22] A. Kocjan, R. Schmidt, A. Lazar, J. Prado-Gonjal, J. Kova˘c, M. Logar, F. J. Mompean, M. Garcia-Hernandez, E. Ruiz-Hitzky, B. Wicklein, In situ generation of 3D graphene-like networks from cellulose nanofibres in sintered ceramics, Nanoscale 10 (2018) 10488–10497, https://doi.org/10.1039/c8nr00717a.

[23] B. Wicklein, A. Kocjan, G. Salazar-Alvarez, F. Carosio, G. Camino, M. Antonietti, L. Bergstr¨om, Thermally insulating and fire-retardant lightweight anisotropic foams based on nanocellulose and graphene oxide, Nat. Nanotechnol. 10 (2015) 277–283, https://doi.org/10.1038/nnano.2014.248.

[24] H. Hudelja, B. Wicklein, D. Ku˘s˘cer, A. Kocjan, Triggering the aqueous interparticle association of γ3Al2O3 hierarchical assemblies using divalent cations and cellulose nanofibers, J. Eur. Ceram. Soc. 41 (2021) 590–598, https://doi.org/10.1016/j. jeurceramsoc.2020.09.014.

[25] Y. Kaburagi, M. Ohoyama, Y. Yamaguchi, E. Shindou, A. Yoshida, N. Iwashita, N. Yoshizawa, M. Kodama, Graphitization behavior of carbon nanofibers derived from bacteria cellulose, Tanso 2012 (2012) 225–230, https://doi.org/10.7209/tanso.2012.225.

[26] K. Rajeswari, M.B. Suresh, U.S. Hareesh, Y.S. Rao, D. Das, R. Johnson, Studies on ionic conductivity of stabilized zirconia ceramics (8YSZ) densified through conventional and non-conventional sintering methodologies, Ceram. Int. 37 (2011) 3557–3564, https://doi.org/10.1016/j.ceramint.2011.05.151.

[27] K. Markandan, J.K. Chin, M.T.T. Tan, Recent progress in graphene based ceramic composites: a review, J. Mater. Res. (2016) 1–23, https://doi.org/10.1557/jmr.2016.390.

[28] C. Ramírez, M. Belmonte, P. Miranzo, M.I. Osendi, Applications of ceramic/graphene composites and hybrids, Materials 14 (2021), https://doi.org/10.3390/ma14082071.

[29] Ú. Fillat, B. Wicklein, R. Martín-Sampedro, D. Ibarra, E. Ruiz-Hitzky, C. Valencia, A. Sarri´on, E. Castro, M.E. Eugenio, Assessing cellulose nanofiber production from olive tree pruning residue, Carbohydr. Polym. 179 (2018) 252–261, https://doi. org/10.1016/j.carbpol.2017.09.072.

[30] M. Mendelson, Average grain size in polycrystalline ceramics, J. Am. Ceram. Soc. 52 (1969) 443–446, http://onlinelibrary.wiley.com/doi/10.1111/j.1151-2916.1969.tb11975.x/abstract (accessed January 7, 2014.

[31] J. Chevalier, L. Gremillard, A.V. Virkar, D.R. Clarke, The tetragonal-monoclinic transformation in zirconia: lessons learned and future trends, J. Am. Ceram. Soc. 92 (2009) 1901–1920, https://doi.org/10.1111/j.1551-2916.2009.03278.x.

[32] A. Nieto, D. Lahiri, A. Agarwal, Graphene nanoplatelets reinforced tantalum carbide consolidated by spark plasma sintering, Mater. Sci. Eng. A 582 (2013) 338–346, https://doi.org/10.1016/j.msea.2013.06.006.

[33] N. Shanbhog, V.K. Bakshi A.N., S.R., Effect of graphene nano-platelet addition on the microstructure and spark plasma sintering kinetics of zirconium diboride, Int. J. Refract. Met. Hard Mater. 84 (2019), https://doi.org/10.1016/j.ijrmhm.2019.104979.

[34] D. Sherman, D. Brandon, Mechanical properties and their relation to microstructure, Adv. Eng. Mater. 1 (1999) 161–181, https://doi.org/10.1002/9783527618217.ch3.

[35] L.M. Malard, M.A. Pimenta, G. Dresselhaus, M.S. Dresselhaus, Raman spectroscopy in graphene, Phys. Rep. 473 (2009) 51–87, https://doi.org/10.1016/j.physrep.2009.02.003.

[36] A. Kaniyoor, S. Ramaprabhu, A Raman spectroscopic investigation of graphite oxide derived graphene, AIP Adv. 2 (2012), https://doi.org/10.1063/1.4756995.

[37] R. Martín-Sampedro, M.E. Eugenio, Ú. Fillat, J.A. Martín, P. Aranda, E. Ruiz-Hitzky, D. Ibarra, B. Wicklein, Biorefinery of lignocellulosic biomass from an Elm clone: production of fermentable sugars and lignin-derived biochar for energy and environmental applications, Energy Technol. 7 (2019) 277–287, https://doi.org/10.1002/ente.201800685.

[38] B. Wicklein, J. Arranz, A. Mayoral, P. Aranda, Y. Huttel, E. Ruiz-Hitzky, Nanostructured carbon-metal hybrid aerogels from bacterial cellulose, RSC Adv. 7 (2017) 42203–42210, https://doi.org/10.1039/c7ra07534k.

[39] V.N. Tsaneva, W. Kwapinski, X. Teng, B.A. Glowacki, Assessment of the structural evolution of carbons from microwave plasma natural gas reforming and biomass pyrolysis using Raman spectroscopy, Carbon N.Y. 80 (2014) 617–628, https://doi. org/10.1016/j.carbon.2014.09.005.

[40] J. Ribeiro-Soares, M.E. Oliveros, C. Garin, M.V. David, L.G.P. Martins, C. A. Almeida, E.H. Martins-Ferreira, K. Takai, T. Enoki, R. Magalh˜aes-Paniago, A. Malachias, A. Jorio, B.S. Archanjo, C.A. Achete, L.G. Cançado, Structural analysis of polycrystalline graphene systems by Raman spectroscopy, Carbon N.Y. 95 (2015) 646–652, https://doi.org/10.1016/j.carbon.2015.08.020.

[41] F. Tuinstra, J.L. Koenig, Raman spectrum of graphite, J. Chem. Phys. 53 (1970) 1126–1130, https://doi.org/10.1063/1.1674108.

[42] A.C. Ferrari, J. Robertson, Interpretation of Raman spectra of disordered and amorphous carbon, Phys. Rev. B. 61 (2000) 14095–14107, https://doi.org/10.1103/PhysRevB.61.14095.

[43] L.G. Can¸ado, K. Takai, T. Enoki, M. Endo, Y.A. Kim, H. Mizusaki, A. Jorio, L. N. Coelho, R. Magalh˜aes-Paniago, M.A. Pimenta, General equation for the determination of the crystallite size La of nanographite by Raman spectroscopy, Appl. Phys. Lett. 88 (2006), https://doi.org/10.1063/1.2196057.

[44] L.G. Cançado, K. Takai, T. Enoki, M. Endo, Y.A. Kim, H. Mizusaki, N.L. Speziali, A. Jorio, M.A. Pimenta, Measuring the degree of stacking order in graphite by Raman spectroscopy, Carbon N.Y. 46 (2008) 272–275, https://doi.org/10.1016/j.carbon.2007.11.015.

[45] V.N. Tsaneva, W. Kwapinski, X. Teng, B.A. Glowacki, Assessment of the structural evolution of carbons from microwave plasma natural gas reforming and biomass pyrolysis using Raman spectroscopy, Carbon N.Y. 80 (2014) 617–628, https://doi. org/10.1016/j.carbon.2014.09.005.

[46] A. Merlen, J.G. Buijnsters, C. Pardanaud, A guide to and review of the use of multiwavelength raman spectroscopy for characterizing defective aromatic carbon solids: from graphene to amorphous carbons, Coatings 7 (2017), https://doi.org/ 10.3390/coatings7100153.

[47] M.S. Dresselhaus, A. Jorio, A.G. Souza Filho, R. Saito, Defect characterization in graphene and carbon nanotubes using Raman spectroscopy, Philos. Trans. R. Soc. A Math. Phys. Eng. Sci. 368 (2010) 5355–5377, https://doi.org/10.1098/rsta.2010.0213.

[48] A. Cuesta, P. Dhamelincourt, J. Laureyns, A. Martínez-Alonso, J.M.D. Tasc´on, Raman microprobe studies on carbon materials, Carbon N.Y. 32 (1994) 1523–1532, https://doi.org/10.1016/0008-6223(94)90148-1.

[49] A.G. Dumanlı, A.H. Windle, Carbon fibres from cellulosic precursors: a review, J. Mater. Sci. 47 (2012) 4236–4250, https://doi.org/10.1007/s10853-011-6081-8.

[50] D.-Y. Kim, Y. Nishiyama, M. Wada, S. Kuga, Graphitization of highly crystalline cellulose, Carbon N.Y. 39 (2001) 1051–1056, https://doi.org/10.1016/S0008-6223(00)00221-9.

[51] O. Ishida, D.-Y. Kim, S. Kuga, Y. Nishiyama, R.M. Brown, Microfibrillar carbon from native cellulose, Cellulose 11 (2004) 475–480, https://doi.org/10.1023/B:CELL.0000046410.31007.0b.

[52] L. Deng, R.J. Young, I.A. Kinloch, Y. Zhu, S.J. Eichhorn, Carbon nanofibres produced from electrospun cellulose nanofibres, Carbon N.Y. 58 (2013) 66–75, https://doi.org/10.1016/j.carbon.2013.02.032.

[54] B.J.T.S. Irvine, D.C. Sinclair, A.R. West, Electroceramics characterisation by impedance sepctroscopy.pdf, Arch. Fr. Pediatr. 42 (1985) 575–576.

[55] R. Schmidt, Ceramic Materials Research Trends, Novascience Publishers, Hauppauge (USA), 2007.

[56] E. Barsoukov, J. Macdonald (Eds.), Impedance Spectroscopy: Theory Experiment, and Applications, Wiley, 2018.

[57] O.Y. Kurapova, A.G. Glukharev, O.V. Glumov, M.Y. Kurapov, E.V. Boltynjuk, V. G. Konakov, Structure and electrical properties of YSZ-rGO composites and YSZ ceramics, obtained from composite powder, Electrochim. Acta 320 (2019), 134573, https://doi.org/10.1016/j.electacta.2019.134573.

[58] C. Ahamer, A.K. Opitz, G.M. Rupp, J. Fleig, Revisiting the temperature dependent ionic conductivity of Yttria Stabilized Zirconia (YSZ), J. Electrochem. Soc. 164 (2017) F790–F803, https://doi.org/10.1149/2.0641707jes.

[59] Z. Gao, L.V. Mogni, E.C. Miller, J.G. Railsback, S.A. Barnett, A perspective on low-temperature solid oxide fuel cells, Energy Environ. Sci. 9 (2016) 1602–1644, https://doi.org/10.1039/c5ee03858h.

[60] K. Ahmad, M.A. Ahmad, R. Raza, M.A. Khan, Z.U. Rehman, G. Abbas, Graphene incorporated nanocomposite anode for low temperature SOFCs, J. Electron. Mater. 48 (2019) 7507–7514, https://doi.org/10.1007/s11664-019-07589-6.